Catalysis Science & Technology

rsc.li/catalysis
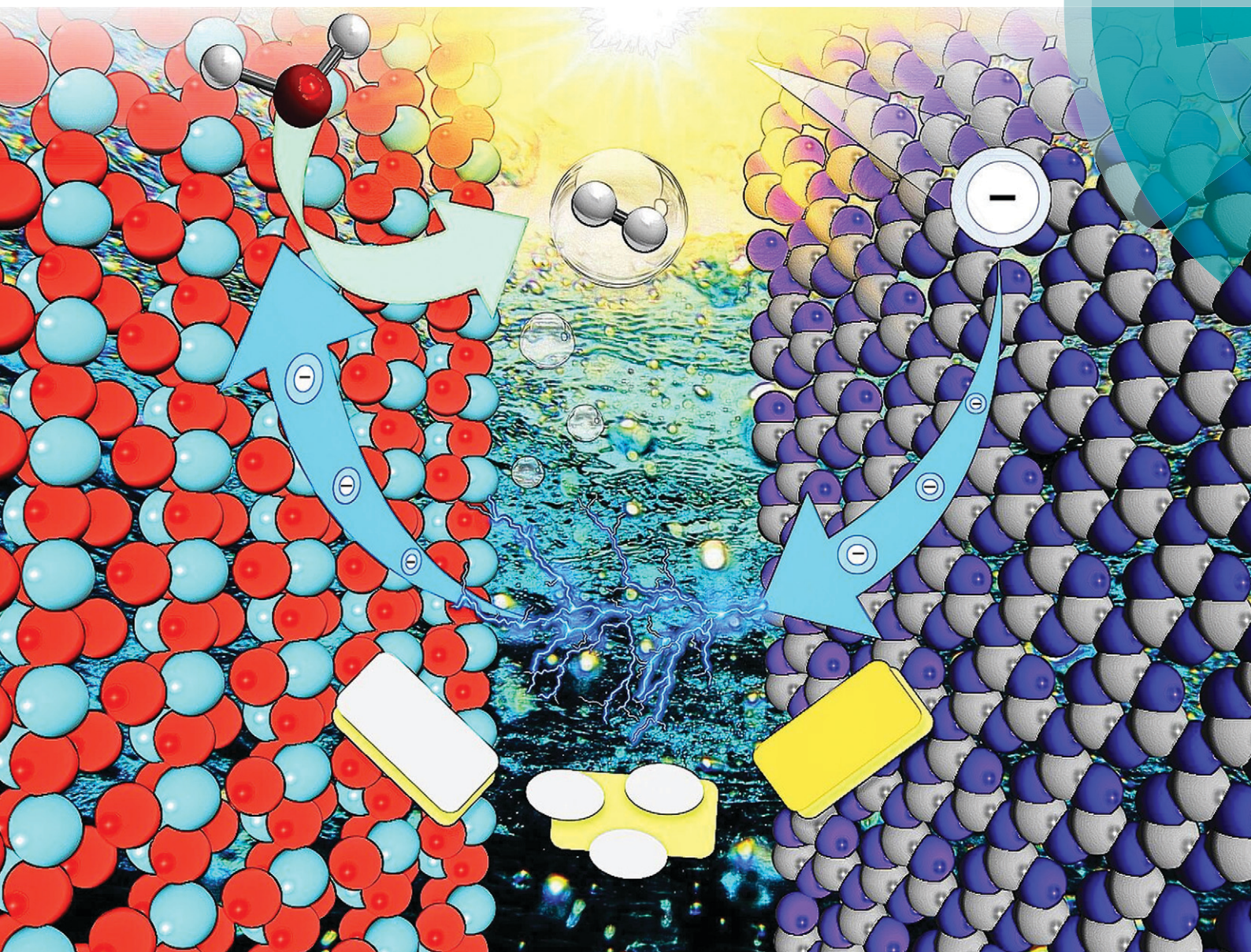
ROYAL SOCIETY OF CHEMISTRY | Celebrating IYPT 2019

PAPER
Limin Huang, Meng Gu *et al.*
Comparison of TiO_2 and $g-C_3N_4$ 2D/2D nanocomposites from three synthesis protocols for visible-light induced hydrogen evolution

PAPER

Check for updates

Comparison of TiO$_2$ and g-C$_3$N$_4$ 2D/2D nanocomposites from three synthesis protocols for visible-light induced hydrogen evolution†

Ruyi Zhong,[ab] Zisheng Zhang,[a] Shuqi Luo,[a] Z. Conrad Zhang, [iD][b] Limin Huang*[a] and Meng Gu [iD]*[c]

Knowledge of the interfacial structure of nanocomposite materials is a prerequisite for rational design of nanostructured photocatalysts. Herein, TiO$_2$ and g-C$_3$N$_4$ 2D/2D nanocomposites were fabricated from three distinct synthetic protocols (*i.e.*, co-calcination, solvothermal treatment and charge-induced aggregation), showing different degrees of enhancement (1.4–6.1 fold) in the visible-light induced photocatalytic hydrogen evolution reaction compared to the simple physical mixture. We propose that the interfacial Ti–O–N covalent bonding promotes the charge carrier transfer and separation more effectively than the electrostatic interaction, thus accelerating the photocatalytic H$_2$ production. Meanwhile, the exposed surface area of TiO$_2$ in the composite needs to be enlarged for deposition of the co-catalyst. This research sheds light on the rational design of hybrid nanocomposites based on earth-abundant elements for photocatalysis.

Introduction

Hydrogen is a promising clean energy carrier, as an environmentally friendly alternative to conventional fossil fuels, owing to its high combustion energy and zero emission.[1–3] Photocatalytic water splitting using solar energy by semiconductor photocatalysts has received intensive research interest in recent decades.[4,5] Fujishima and Honda originally proposed non-toxic TiO$_2$ as a stable benchmark photocatalyst under UV irradiation.[6] However, the large bandgap of TiO$_2$ (*ca.* 3.2 eV) restricts its utilization of the whole solar spectrum, as UV light accounts for only a proportion of 4% and visible light (400–800 nm) is dominant (50%). Doping TiO$_2$ with various elements or self-doping with Ti^{3+} could extend its optical absorption to the visible-light range, which, however, usually suffers from rapid photogenerated electron–hole recombination and reduced stability of the doped materials.[7,8]

Recently, g-C$_3$N$_4$ has been identified as a promising organic semiconductor for photocatalytic applications, including photoreduction of H$_2$O to H$_2$.[5,9–14] Bulk g-C$_3$N$_4$ prepared

from facile pyrolysis of nitrogen-rich precursors has a suitable band structure with a low band gap of *ca.* 2.7 eV to harvest visible light, but its photocatalytic performance is limited by its low surface area and fast recombination rate of photogenerated charge carriers.[12–17] Exfoliation of g-C$_3$N$_4$ to 2D nanosheets by various chemical and physical approaches could increase the surface area and reduce the charge recombination, but the problem of re-stacking remains.[9,10,12,13]

Constructing heterojunction structures of TiO$_2$ and g-C$_3$N$_4$ has been proven as a cost-effective way to avoid the above drawbacks of each component and realize a synergic effect in promoting the efficient generation and separation of charge carriers, thus boosting the photocatalytic activity.[12,18,19] The heterostructure interfaces would offer a premise for such synergism during photocatalytic reactions by forming different types of band diagrams.[12,18,19] Therefore many efforts have been made to fabricate TiO$_2$ with g-C$_3$N$_4$ to form a composite with abundant heterostructure interfaces. Most of the fabrication processes of heterostructures are based on simultaneous formation of heterojunctions and one (or both) of the components.[20–31] For instance, solvothermal synthesis of nanostructured TiO$_2$ has been performed in the presence of pre-synthesized bulk g-C$_3$N$_4$,[20] thermally exfoliated g-C$_3$N$_4$,[22,23] oxidized g-C$_3$N$_4$,[21,24] or protonated g-C$_3$N$_4$,[25] forming particles attached onto sheets[20–23] or nanosheet to nanosheet assemblies,[24,25] outperforming bare TiO$_2$ or g-C$_3$N$_4$ in photocatalytic reactions. The precursors for g-C$_3$N$_4$ can be mixed with the preformed TiO$_2$[28,29,31] or its precursors[26,27,30] to undergo calcination[26–30] or refluxing,[31] forming core–shell[29,31] or

[a] *Department of Chemistry, Southern University of Science and Technology, Shenzhen, 518055, China. E-mail: huanglm@sustc.edu.cn*
[b] *Dalian Institute of Chemical Physics, Chinese Academy of Sciences, Dalian 116023, China*
[c] *Department of Materials Science and Engineering, Southern University of Science and Technology, Shenzhen, 518055, China. E-mail: gum@sustc.edu.cn*
† Electronic supplementary information (ESI) available: The results of TGA and N$_2$ sorption measurements, SEM and low-magnification TEM images, and stability test results. See DOI: 10.1039/c8cy00965a

This journal is © The Royal Society of Chemistry 2019

Catal. Sci. Technol., 2019, **9**, 75–85 | 75

particle attached to sheet[26–28] structures with improved photocatalytic activity. As for the as-formed binary components, co-calcination has been frequently applied, resulting in particle on nanosheet g-C_3N_4/TiO_2 structures.[32–34] In addition, charge-induced aggregation has been proposed for constructing intimate heterojunctions of 0D/2D Nb_2O_5/g-C_3N_4,[15] 2D/2D g-C_3N_4/graphene oxide,[36] 2D/2D graphene/$SnNb_2O_6$,[37] *etc.* Among the various morphologies, the 2D/2D heterojunction has unique merits compared with the 0D/1D, 1D/1D, 0D/2D and 1D/2D interfaces, owing to the increased contact region and the intimate interface regardless of the lattice mismatch, as well as the large lateral size with high surface area, to promote charge transfer and electron–hole separation, thereby improving the photocatalytic performance.[19,24,25,36,37] Meanwhile, the formation of 2D/2D heterostructures is also beneficial for the catalyst stability against photocorrosion and agglomeration.[19,24,25,36,37] However, relatively scarce studies have been reported concerning fabrication of 2D/2D heterostructures of TiO_2 and g-C_3N_4,[24,25] let alone comparison of different construction approaches and clarification of the interfacial interaction modes.

Moreover, a third component has been frequently involved to form a ternary composite,[38–42] for example metallic Ag was incorporated into g-C_3N_4/TiO_2 to facilitate interfacial electron transfer,[38] Cu into MoO_3/g-C_3N_4 to boost visible light absorption for the surface plasmon resonance effect,[39] Al_2O_3 into g-C_3N_4/ZnO to remedy the lattice mismatch,[40] *etc.* Nevertheless, ternary nanocomposites bring in larger complexity than binary nanocomposites, due to their more intricate interfaces.

Herein, we investigated differently fabricated TiO_2 and g-C_3N_4 2D/2D nanocomposites for efficient and stable photocatalytic H_2 evolution under visible-light irradiation. The preparation methods, *in situ* solvothermal treatment, co-calcination and charge-induced aggregation, were adopted with the aim of finely tuning the interfacial properties for the facilitation of electron–hole separation and electron transfer. By analyzing the photocatalytic performance and the physico-chemical properties of each type of composite, formation of interfacial covalent Ti–O–N bonds is more favorable than electrostatic interactions for promoting electron transfer and suppressing charge recombination. Meanwhile, large surface area of the composite needs to be ensured for abundant deposition of the co-catalyst.

Experimental

Materials

A poly(ethylene oxide)-*block*-poly(propylene oxide)-*block*-poly(ethylene oxide) triblock copolymer (Pluronic P123, $EO_{20}PO_{70}PEO_{20}$, M_W = 5800) was purchased from Sigma-Aldrich (USA). Titanium isopropoxide (TTIP), hydrochloric acid, ethylene glycol, melamine, ethanol, sodium borohydride, H_2PtCl_6 and triethanolamine (TEOA) were purchased from Aladdin Industrial Corporation (Shanghai, China). All reagents were used as-received without further purification.

Synthesis of raw TiO_2 and g-C_3N_4

The ultrathin TiO_2 nanosheets were prepared using a solvothermal self-assembly method.[24,43] Namely, 200 mg of raw TiO_2 was ground thoroughly with 200 mg of $NaBH_4$ at room temperature. The mixture was transferred to a porcelain boat and heated in a N_2 flow at 220 °C for 20 min with a ramp rate of 10 °C min^{-1}. The product was collected, washed with H_2O to remove excess $NaBH_4$ and dried at 60 °C overnight.

The modification of g-C_3N_4 was performed by hydrothermal treatment[45] or acid treatment[46] to generate O–CN and H–CN, respectively. Briefly, for O–CN, 200 mg of g-C_3N_4 was dispersed in 100 mL H_2O by ultrasonication for 30 min and transferred to a 200 mL Teflon-lined autoclave for heating at 180 °C for 4 h. The solid sample was collected by centrifugation, washed with H_2O and dried at 60 °C overnight. For H–CN, 500 mg of g-C_3N_4 was mixed with 12.5 mL of concentrated HCl (37.5 wt%) at room temperature under stirring for 1 h. The solid sample was collected by centrifugation, washed with H_2O to remove excess HCl and dried at 60 °C overnight.

Fabrication of three TiO_2 and g-C_3N_4 nanocomposites

Method I. The bottom-up synthesis method of solvothermal *in situ* growth of TiO_2 nanosheets on O–CN was used.[24] The protocol of precursor solution containing TTIP and P123 was the same as the synthesis of the raw TiO_2 nanosheets. 100 mg of O–CN was dispersed in 40 mL ethylene glycol by ultrasonication for 30 min. 5 mL of precursor solution was mixed with the above O–CN suspension and transferred to a 100 mL Teflon-lined autoclave for heating at 150 °C for 20 h. The yellow precipitates were extensively washed with ethanol and dried at 60 °C overnight to obtain the final product O–CN/TiO_2.

Method II. Co-calcination of raw TiO_2 nanosheets with CN was applied, aiming at utilizing the thermal exfoliation of bulk g-C_3N_4.[22,33,34,47] 100 mg of raw TiO_2 and 100 mg of CN were added to 5 mL of ethanol and the resultant suspension was vigorously stirred at room temperature for 1 h and ultrasonicated for 20 min. The powder from drying the milky mixture at 60 °C overnight was placed in a covered porcelain boat for calcination in air at 450 °C for 2 h with a ramp rate of 10 °C min^{-1}. The targeted product was denoted as CN/TiO_2-cal.

Method III. Charge-induced aggregation of H–TiO_2 and H–CN was performed to form intimate contact at the heterojunction with the driving force of electrostatic interaction. 100 mg of proton-functionalized g-C_3N_4 (H–CN), whose zeta-potential was positive when dispersed in H_2O,[36] and 100 mg of $NaBH_4$-reduced TiO_2 nanosheets (H–TiO_2) were dispersed in 100 mL H_2O, respectively, under ultrasonication for 1 h. Then the two suspensions were mixed and ultrasonicated in an ice bath for 2 h to achieve homogeneous suspension. Note that the pH changes were insignificant during the whole experiment and the final pH was still neutral. The material was

76 | *Catal. Sci. Technol.*, 2019, **9**, 75–85

This journal is © The Royal Society of Chemistry 2019

centrifuged and dried at 60 °C overnight to yield the final product H–CN/H–TiO$_2$.

As a control, 100 mg of raw TiO$_2$ was ground manually with 100 mg of O–CN, and the resultant sample was denoted as "O–CN TiO$_2$ mixed".

Characterization

Zeta potentials were obtained by dynamic light-scattering analysis using a Zetasizer Nano ZS90 analyzer. 20 mg of each sample was dispersed in 50 mL of H$_2$O by ultrasonication for the zeta potential analysis. Thermogravimetric (TGA) measurements were performed in a Mettler-Toledo TGA instrument. About 10 mg of each sample was placed in an alumina crucible and heated to 800 °C at a heating rate of 10 °C min^{-1} in an air flow. X-ray diffraction (XRD) patterns were acquired on a Rigaku Smartlab-9 kW X-ray diffractometer in the 2θ range from 5 to 80° and at a scan speed of 5° min^{-1}. Fourier transform infrared spectra (FTIR) were recorded on a Bruker IFS 66 spectrometer with 128 scans at a resolution of 2 cm^{-1}. The samples were finely ground with KBr for the transparent pellets. The specific surface area and pore structure of each sample were determined by nitrogen sorption analysis using a Micromeritics ASAP 2020. Scanning electron microscopy (SEM) images were obtained on a Tescan MIRA3 scanning electron microscope. Transmission electron microscopy (TEM) images were acquired on a JEM-2100 electron microscope operating at 200 kV. The samples for TEM were prepared by depositing an ethanolic suspension of each sample onto holey carbon-coated copper grids and drying. The electron microscopy data (EDS, HAADF STEM) were acquired using a Cs aberration-corrected FEI Titan Themis G2 at 200 kV equipped with an ultra-high brightness gun and super-X EDS detector. X-ray photoelectron spectroscopy (XPS) measurement was carried out with a Thermo SCIENTIFIC ESCALAB 250Xi instrument using monochromatized Al Kα as the excitation source. The C 1s signal at 284.8 eV was used to calibrate the binding energy (BE) and a Shirley-type background was applied for each spectrum. UV-vis diffuse reflectance spectra (UV-vis DRS) of the samples were recorded using a Lambda 950 UV/vis/NIR spectrometer (Perkin Elmer) equipped with a diffuse reflectance attachment of a Spectralon-coated integrating sphere against a BaSO$_4$ reference. Photoluminescence (PL) spectra were collected on a fluorescence spectrometer (Horiba PTI QuantaMaster 400) at room temperature with a laser excitation wavelength of 330 nm.

Photocatalytic testing

The photocatalytic hydrogen evolution reactions were performed using an online photocatalytic hydrogen generation system (CEL-SPH2N, AuLight, Beijing). A 300 W Xe lamp (CEL-HX300) equipped with a UV cut-off filter (UVIRCUT400, AuLight, Beijing, $\lambda > 400$ nm) was used as the visible light source, which was fan-cooled during the experiment. To maintain the ambient temperature of the reaction system un-

der irradiation, a liquid trap system with water circulation was used. In a typical test, 50 mg of photocatalyst was dispersed in 50 mL of aqueous solution containing 20 vol% TEOA as a sacrificial reagent. 3 wt% Pt co-catalyst was photo-deposited uniformly onto the surface of the photocatalyst using H$_2$PtCl$_6$ as a precursor. Before irradiation, the suspension was degassed thoroughly by evacuation to remove dissolved gases. After an adequate photo-deposition period, the gaseous product was analyzed every hour. H$_2$ evolution was quantitatively determined by online gas chromatography (GC-7890, thermal conductivity detector, molecular sieves 5 Å, N$_2$ carrier, Yiyou, Shanghai).

Results and discussion

Structural characterization of catalysts

Scheme 1 illustrates the three composite samples (O–CN/TiO$_2$, CN/TiO$_2$-cal and H–CN/H–TiO$_2$) and their precursors (TiO$_2$, TiO$_2$-cal, H–TiO$_2$, CN, O–CN and H–CN) investigated in this article. The solvothermal *in situ* growth fabrication approach was detailed in our previous work.[24] Ultrathin TiO$_2$ nanosheets are formed *in situ* by P123 template-assisted self-assembly and are attached to the edges of O–CN where oxygenated groups exist *via* Ti–O–N covalent linkages.[24] The as-formed Ti–O–N bonds under solvothermal treatment have been demonstrated to facilitate the efficient charge separation at interfaces and enhance the photocatalytic H$_2$ evolution activity. However, this composite still has residual P123 which may interfere with the charge and mass transfer in the photocatalytic process.[25] Besides, other interaction modes of the interface of TiO$_2$ and g-C$_3$N$_4$ for instance electrostatic Coulombic force and the influence of the exfoliation degree of g-C$_3$N$_4$ remain to be explored. Therefore, two distinct and versatile approaches, *i.e.* co-calcination and charge-induced self-assembly, were also applied, to further investigate the contribution of the architecture of the interface to the photocatalytic hydrogen evolution reaction. During co-calcination, the thermal exfoliation of g-C$_3$N$_4$,[22,33,34,47] the removal of P123 organic residues[25,48] and the increased crystallinity[25,48] are expected, which could be beneficial for the formation of close 2D/2D interfacial contact. During surface charge-
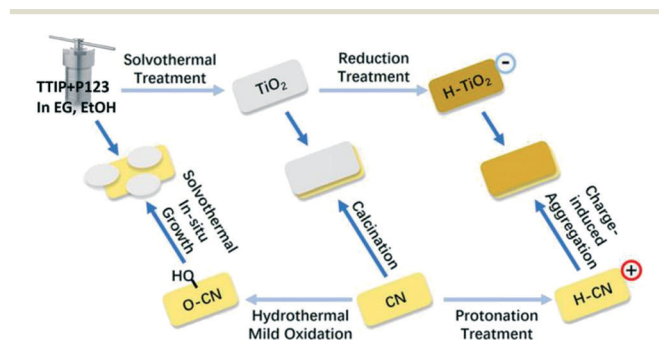
Scheme 1 Schematic illustration of the three synthesis approaches for forming three composite samples (O–CN/TiO$_2$, CN/TiO$_2$-cal and H–CN/H–TiO$_2$).

This journal is © The Royal Society of Chemistry 2019

Catal. Sci. Technol., 2019, **9**, 75–85 | 77

induced aggregation, the oppositely-charged nanosheets could result in improved interaction between TiO_2 and g-C_3N_4 and thus, the charge transfer across the hetero-junction to promote the photocatalytic activity.[15,36,37]

The TGA/DTG curves of the three composite samples (O–CN/TiO_2, CN/TiO_2-cal and H–CN/H–TiO_2), the physically mixed sample (O–CN TiO_2 mixed) and the precursors (TiO_2, H–TiO_2, CN, O–CN and H–CN) are shown in Fig. S1.† For the nanocomposites, aside from the H_2O desorption peak below 200 °C, the sharp DTG peak at about 300 °C is assigned to the P123 residues,[24,25,48] and the peak starting from about 450 °C is due to the burn-off of g-C_3N_4 species. The weight losses at different temperature stages are summarized in Table 1. The similar weight percentages of g-C_3N_4 species for the three nanocomposites and the simple physical mixture rationalize the comparison of the physicochemical properties among these materials. The amount ratio of g-C_3N_4 to TiO_2 is roughly 1:1 in all the composites in this work; the 1:1 ratio has been found to be the optimized value for the construction of heterojunctions in the O–CN/TiO_2 sample (g-C_3N_4 to TiO_2 ratios of 1:1, 1:2 and 2:1 were investigated) without compromising the large surface area.[24] It is also noteworthy that the content of P123 residues decreases to zero, following the order O–CN/TiO_2, H–CN/H–TiO_2 and CN/TiO_2-cal.

Table 1 also lists the textural properties of the composites and the precursors. The N_2 sorption isotherms and pore size distributions are plotted in Fig. S2.† All the materials present type IV isotherms with H4 type hysteresis loops, which are caused by the stacking of nanosheets forming slit-like pores. The raw TiO_2 shows a large surface area of 330 m^2 g^{-1}, while pristine CN shows an S_{BET} of only 12 m^2 g^{-1}. The average pore size of CN is much larger than that of TiO_2. These results indicate that the solvothermally synthesized TiO_2 is highly exfoliated and of relatively small sheet size, while CN is largely bulky. The O–CN and H–CN increase the surface area to 55 and 19 m^2 g^{-1}, respectively, proving the delamination effect during these treatments.[45,46] After formation of

heterojunctions with TiO_2 in the three distinct ways, the surface areas increase tremendously to 73, 263 and 163 m^2 g^{-1} for CN/TiO_2-cal, O–CN/TiO_2 and H–CN/H–TiO_2, respectively. The surface area of the composite is mainly contributed by the TiO_2 component. The high surface area of O–CN/TiO_2 implies the successful formation of ultrathin TiO_2 nanosheets under solvothermal conditions in the presence of O–CN. The high surface area would supply more photocatalytically reactive centers to speed up the hydrogen evolution reaction. Besides, CN/TiO_2-cal possesses merely mesopores (V_{meso} = 0.30 cm^3 g^{-1}), whereas H–CN/H–TiO_2 shows a V_{micro} of 0.04 cm^3 g^{-1} out of the V_{tot} of 0.17 cm^3 g^{-1}. These results suggest the different origins of the slit-like pores. It is likely that the mesopores in CN/TiO_2-cal are from the vacancy after the removal of P123 residues and the stacking of the nanosheets. As for H–CN/H–TiO_2, compact stacking driven by electrostatic Coulombic force can be envisaged, resulting in relatively high microporosity. Moreover, it has been found that very small pores around 2.14 nm in porous g-C_3N_4 from kaolinite-templated synthesis still provided reactive surface area for the photocatalytic hydrogen evolution with Pt as the co-catalyst.[49] Therefore, there may be no diffusion limitation in micropores and the surface area could serve as an evaluation criterion for the amount of photocatalytically reactive centers.

The XRD patterns of the TiO_2 and g-C_3N_4 composites and precursors are shown in Fig. 1. The characteristic peaks corresponding to the (101), (004), (200), (105), (211) and (204) planes of anatase are identified with the XRD database. These diffraction peaks are obvious in TiO_2-cal and CN/TiO_2-cal, whereas the raw TiO_2 sheets, O–CN/TiO_2 and H–CN/H–TiO_2 are largely amorphous in the TiO_2 phase with a minor rutile phase as well. Calcination at 450 °C improves the crystallization degree of TiO_2 nanosheets and transforms them to a pure anatase phase, consistent with a reported observation.[48] In the co-calcined CN/TiO_2-cal, TiO_2 nanosheets also grow into the anatase phase in the presence of CN. For the g-C_3N_4 precursors and the composite samples, the peaks

Table 1 Compositional and textural properties of the TiO_2 and g-C_3N_4 nanocomposites and their precursors

Entry	Catalyst	TiO_2[a] (wt%)	g-C_3N_4 species[b] (wt%)	P123 residues[c] (wt%)	S_{BET}[d] (m^2 g^{-1})	V_{tot}[e] (cm^3 g^{-1})	V_{meso}[f] (cm^3 g^{-1})	Average pore size[g] (nm)
1	TiO_2	59	—	13	330	0.41	0.36	5.0
2	H–TiO_2	68	—	10	n.d.	n.d.	n.d.	n.d.
3	CN	0	99	—	12	0.12	0.12	43.5
4	O–CN	0	98	—	55	0.20	0.20	14.7
5	H–CN	0	90	—	19	0.12	0.12	25.8
6	CN/TiO_2-cal	57	45	0	73	0.30	0.30	16.3
7	O–CN/TiO_2	37	47	8	263	0.57	0.53	8.7
8	H–CN/H–TiO_2	37	50	5	163	0.17	0.13	4.3
9	O–CN TiO_2 mixed	35	48	8	n.d.	n.d.	n.d.	n.d.

[a] Weight percentage of TiO_2 was determined from the plateau in the high temperature range of TGA curves for samples containing TiO_2. [b] Weight percentage of residual P123 was determined from the weight loss around 300 °C of the TGA curves for samples containing TiO_2. [c] Weight percentage of g-C_3N_4 species was determined from the main weight loss above 450 °C of the TGA curves for samples containing g-C_3N_4. [d] Surface area (S_{BET}) was calculated from the N_2 sorption isotherms by the Brunauer–Emmett–Teller (BET) method. [e] Total pore volume (V_{tot}) was calculated from the saturation plateau at high relative pressures. [f] Mesopore volume (V_{meso}) was calculated by subtracting the micropore volume from the V_{tot} using the t-plot method. [g] Pore size (D_{pore}) was calculated from the adsorption branch of the isotherms by the Barrett–Joyner–Halenda (BJH) method.

78 | Catal. Sci. Technol., 2019, 9, 75–85

This journal is © The Royal Society of Chemistry 2019
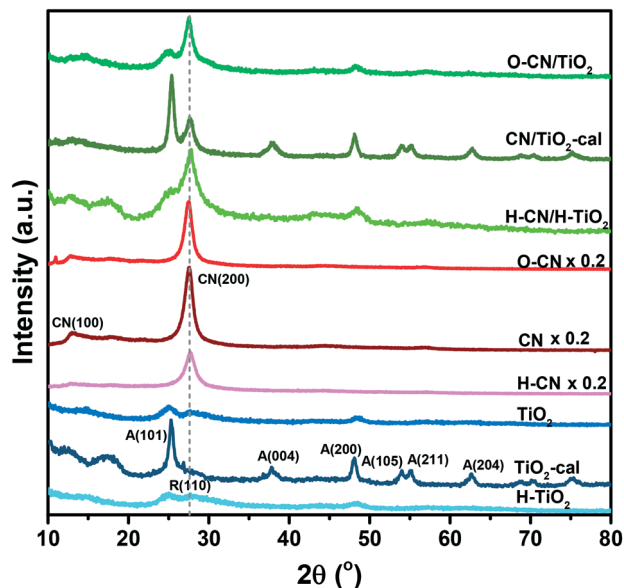
Fig. 1 XRD patterns of the three composite samples (O–CN/TiO$_2$, CN/TiO$_2$-cal and H–CN/H–TiO$_2$) and the precursors (TiO$_2$, TiO$_2$-cal, H–TiO$_2$, CN, O–CN and H–CN). The A, R and CN represent anatase, rutile and g-C$_3$N$_4$, respectively.
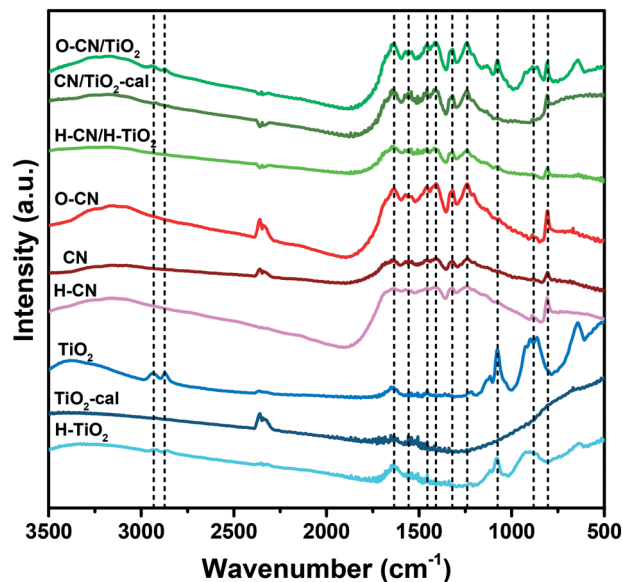
Fig. 2 FTIR spectra of the three composite samples (O–CN/TiO$_2$, CN/TiO$_2$-cal and H–CN/H–TiO$_2$) and the precursors (TiO$_2$, TiO$_2$-cal, H–TiO$_2$, CN, O–CN and H–CN).

corresponding to the (100) and (200) planes of g-C$_3$N$_4$ are observed, attributed to the in-plane repeated tri-s-triazine units and stacking of the conjugated N-containing aromatic ring, respectively.[41] The crystallinity of O–CN is more or less the same as that of CN, while H–CN is less ordered than CN, in terms of the peak intensity of CN(200). The CN(200) for the three composites remains at the same position compared to that for the g-C$_3$N$_4$ precursors and the peak widths are in the objective order of crystallinity of the g-C$_3$N$_4$ part, indicating that the presence of TiO$_2$ did not influence the crystal structure of g-C$_3$N$_4$. The XRD pattern of the composite sample can be treated as superposition of those of individual TiO$_2$ and g-C$_3$N$_4$ precursors.

The FTIR spectra are presented in Fig. 2. For the pristine TiO$_2$ nanosheets, the absorption peak around 1635 cm^{-1} is attributed to O–H bending vibrations.[38] The two small peaks at 2935 and 2868 cm^{-1} are attributed to C–H stretching vibrations of the residual P123 species. These organics also show the C–O stretching vibration and C–H bending vibration signals in the range of 1200–600 cm^{-1}. The hydrogenated TiO$_2$ shows lower intensity for P123 and these absorption bands disappear for the calcined TiO$_2$, in line with the TGA results. For the g-C$_3$N$_4$ precursors (CN, O–CN and H–CN), the characteristic absorption peaks have similar shapes at the same positions. The strong bands in the range of 1650–1200 cm^{-1} are assigned to the typical stretching modes of the tri-s-triazine skeleton ring and the peak at about 800 cm^{-1} to the breathing mode of the triazine units.[45,50] The FTIR spectra of the three composites embody both the characteristic absorption bands of the individual TiO$_2$ and g-C$_3$N$_4$ precursors, indicating the coupling of TiO$_2$ with g-C$_3$N$_4$ for each composite.

The morphology and microstructure of the three nanocomposites and the precursors were studied by TEM, as shown in Fig. 3. The CN, O–CN and H–CN appear to have relatively large and amorphous laminar morphologies, as reported elsewhere.[24,36,46,50] The protonated H–CN and the mildly-oxygenated O–CN show more exfoliated and less integrated sheets than the pristine CN.[24,36,46] The raw TiO$_2$ shows poorly crystallized nanosheets with a thickness of ca. 1 nm and lengths of ca. 80 nm, consistent with a previous report.[43] The calcination at 450 °C preserves the lamellar structure of the TiO$_2$ sheets; the clear lattice fringe in the magnified region demonstrates the high degree of crystallization. Hydrogenated H–TiO$_2$ shows the crystallinity between raw TiO$_2$ and TiO$_2$-cal, also with the presence of the anatase phase. Notably, the TiO$_2$ nanosheets in H–TiO$_2$ are more corrugated, perhaps due to the mutual electrostatic repulsive force between the negatively charged sites in H–TiO$_2$.[36] The TEM images of the three composites do not clearly show the interface of TiO$_2$ and g-C$_3$N$_4$, but the facts that the lattice fringes belong to anatase TiO$_2$ and the size of g-C$_3$N$_4$ sheets is relatively large help to distinguish the TiO$_2$ from g-C$_3$N$_4$ phases. The SEM and low-magnification TEM images in Fig. S3† both reflect that TiO$_2$ nanosheets were attached onto large O–CN nanosheets in the O–CN/TiO$_2$ nanocomposite. The crystallinity of O–CN/TiO$_2$, H–CN/H–TiO$_2$ and CN/TiO$_2$-cal roughly follows the order of the corresponding pure TiO$_2$, in line with the XRD results. All the three nanocomposites show the intertwined TiO$_2$ and g-C$_3$N$_4$ regions under HRTEM, proving the close linkages and the compacted interfaces for the three distinct fabrication ways.

This journal is © The Royal Society of Chemistry 2019

Catal. Sci. Technol., 2019, 9, 75–85 | 79
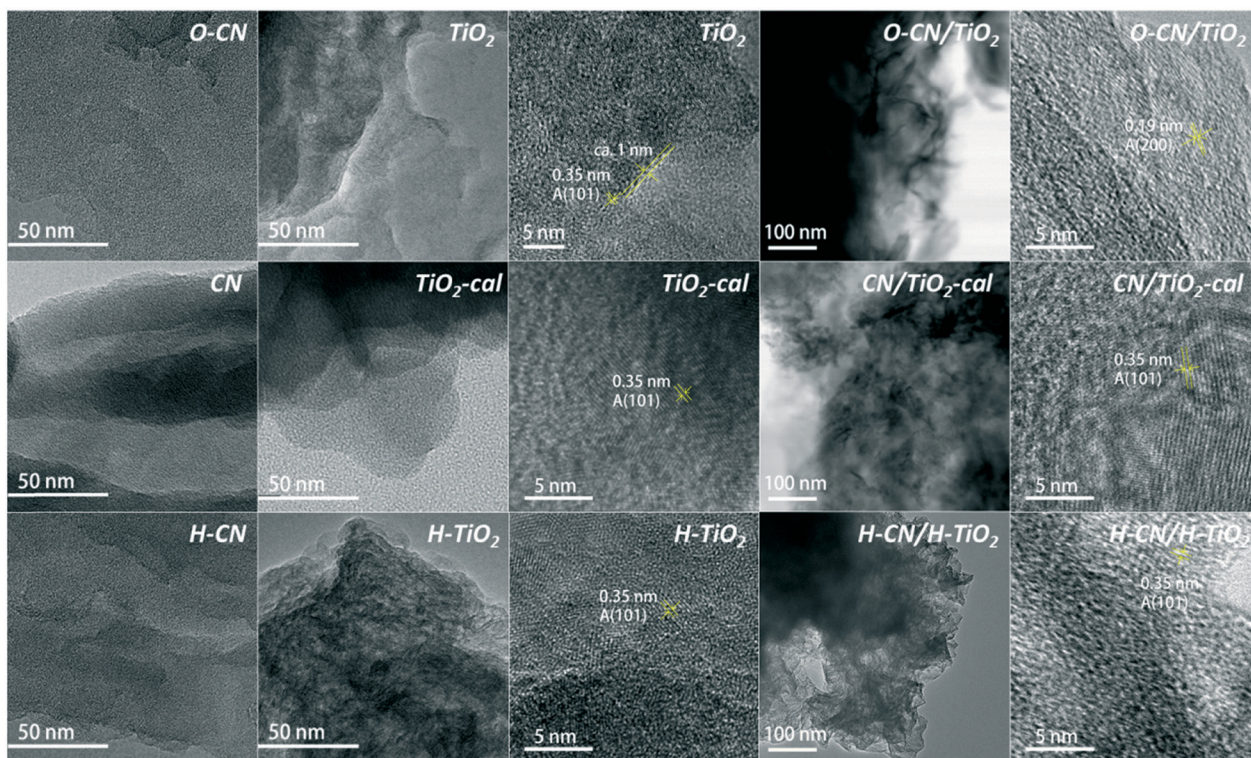
Fig. 3 TEM images of the three composite samples (O–CN/TiO$_2$, CN/TiO$_2$-cal and H–CN/H–TiO$_2$) and the precursors (TiO$_2$, TiO$_2$-cal, H–TiO$_2$, CN, O–CN and H–CN).

High-angle annular dark-field scanning TEM (HAADF-STEM) and energy-dispersive X-ray spectroscopy (EDS) mapping are employed to ascertain the heterojunction structure and composition in the three nanocomposites, as shown in Fig. 4. From the distributions of the four elements C, N, O and Ti and their combined STEM image, O–CN/TiO$_2$ clearly shows many small ultrathin TiO$_2$ nanosheets bonded to the edges of large O–CN sheets, as observed before.[24] TiO$_2$ nanosheets are relatively individually standing on the O–CN sheets, due to the P123 templating effect during solvothermal *in situ* growth synthesis. The interfacial Ti–O–N covalent bonds in O–CN/TiO$_2$ have been demonstrated by EDS point analysis.[24] In the co-calcined nanocomposite, though the TiO$_2$ phase is also in intimate contact with CN sheets, the self-aggregation of TiO$_2$ nanosheets is quite severe, which is attributed to the removal of intercalating P123 residues. In the case of H–CN/H–TiO$_2$, the distributions of C, N, O and Ti are almost the same throughout the whole selected area. The 2D features of H–TiO$_2$ and H–CN are well-preserved, and the charge-directed heteroaggregation upon ultrasonication results in effective formation of heterojunctions. The positively charged H–CN (with a zeta potential equal to 5.5 mV in H$_2$O) is likely to stack alternately with the negatively charged H–TiO$_2$ (with a zeta potential equal to −39.2 mV in H$_2$O) into a layered 2D/2D heterostructure.

XPS was utilized to investigate the oxidation state and surface chemical compositions of the three TiO$_2$ and g-C$_3$N$_4$ nanocomposites, and bare TiO$_2$ and CNs, as shown in Fig. 5.

The C–H and C–C signals of C 1s from adventitious carbon were set to 284.8 eV for calibration. The O–CN/TiO$_2$, H–CN/H–TiO$_2$ and raw TiO$_2$ nanosheets all exhibit Ti 2p$_{3/2}$ and Ti 2p$_{1/2}$ with binding energies at 458.8 and 464.5 eV, respectively, ascribed to Ti^{4+} species in the nanosheets with the presence of residual P123. The presence of Ti^{3+} after NaBH$_4$ reduction hardly causes the alteration in the Ti 2p XPS spectra.[44] The peak positions are lower than those of the reference anatase (Ti 2p$_{3/2}$ = 459.4 eV, Ti 2p$_{1/2}$ = 465.3 eV) or rutile (Ti 2p$_{3/2}$ = 459.3 eV, Ti 2p$_{1/2}$ = 465.3 eV) phases.[43] The CN/TiO$_2$-cal shows a small component peak at 458.8 eV for Ti 2p$_{3/2}$, while the main component peak is at 460.1 eV, showing a shift of 1.3 eV to the higher binding energy, indicating the formation of bulky TiO$_2$ species in the calcined sample.[44,48]

The N 1s XPS spectrum shows four peaks at *ca.* 398.4, 399.0, 399.8 and 401.1 eV in bare CN, corresponding to N atoms in C–N=C, N–(C)$_3$, N–O and N–H, respectively.[24,29] After hydrothermal treatment, the N–O component increases in the N 1s peak, attributed to the introduction of oxygen. The acid treatment would not change the positions of the component peaks but would lead to the increase of the N–H content.[46] After hybridization of g-C$_3$N$_4$ with TiO$_2$, the peak for N–O shifts toward the high binding energy region to different degrees in the three nanocomposites, indicative of the bonding state of the heterojunction. O–CN/TiO$_2$ shows a shift of around 0.4 eV, indicating the formation of Ti–O–N covalent bonds, due to the partial substitution of Ti–O–N with H–O–N and the resultant reduced electron density for the relatively

80 | *Catal. Sci. Technol.*, 2019, **9**, 75–85

This journal is © The Royal Society of Chemistry 2019
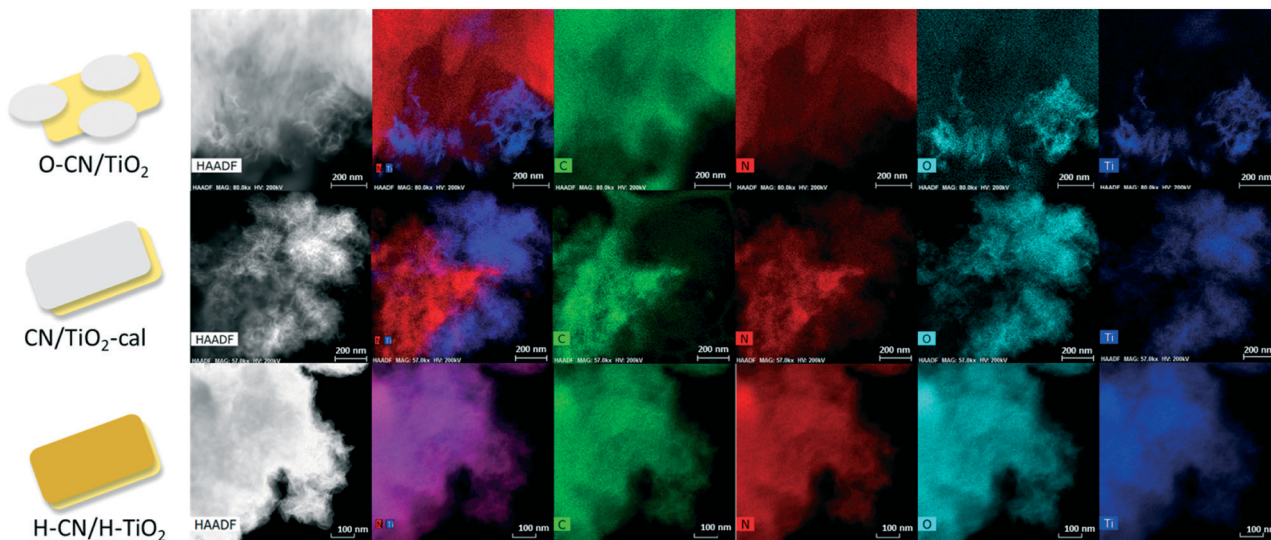
Fig. 4 HADDF STEM images and EDS elemental mapping images of C, N, O and Ti of the three nanocomposites (O–CN/TiO$_2$, CN/TiO$_2$-cal and H–CN/H–TiO$_2$).

electron-deficient Ti atoms. CN/TiO$_2$ shows an even larger shift, *ca.* 0.5 eV, owing to the formation of Ti–O–N covalent bonds and the removal of P123 during the calcination procedure. In contrast, H–CN/H–TiO$_2$ shows only a shift of about 0.1 eV, in good accordance with the subtle change in the N 1s peak positions of 3CN : 1Nb heterostructure prepared from the charge-induced aggregation of Nb$_2$O$_5$ and g-C$_3$N$_4$.[15]

The C 1s spectrum of CN is mainly composed of two peaks at 284.8 and 288.2 eV; the latter peak corresponds to N–C≡N in the triazine rings of g-C$_3$N$_4$.[15,29] The small peak at *ca.* 286.0 eV is assigned to C–(N)$_3$ species.[29] The C 1s spectrum of TiO$_2$ reflects the presence of P123 residues, which are slightly oxidized after the solvothermal synthesis. The nanocomposites of TiO$_2$ and g-C$_3$N$_4$ show the peak at 288.2 eV fea-

turing the N–C≡N of g-C$_3$N$_4$ and the peak at about 286.0 eV, combining the C–(N)$_3$ groups of g-C$_3$N$_4$ and the C–O groups in P123 residues from the TiO$_2$ part.

The O 1s peak in CN and O–CN is located at *ca.* 532.7 eV, arising from the C–O or N–O groups in g-C$_3$N$_4$. O–CN shows a higher amount of O than CN. As for the TiO$_2$ nanosheets, O 1s peaks at 530.6 eV and 532.2 eV are identified, attributed to C–O from P123 residues and Ti–O, respectively. O–CN/TiO$_2$ and H–CN/H–TiO$_2$ show similarly two peaks for O atoms. However, CN/TiO$_2$-cal exhibits two peaks for Ti–O with a distance of 1.4 eV and an area ratio of 4.7 (close to 4.9, the area ratio of the two peaks in Ti 2p). The blue shift of the main Ti–O peak is also likely due to the removal of P123 and the increased crystallinity. Meanwhile, the peak for O–C and O–N in CN/TiO$_2$-cal shifts around 0.4 eV to high binding energy relative to CN, possibly resulting from the formation of Ti–O–N covalent bonds as a consequence of the relatively small electronegativity of Ti compared with H. O–CN/TiO$_2$ should have such shifts as well, though these are overlapped by the O 1s signals from residual P123.

Photospectral analysis and photocatalytic hydrogen evolution performance of catalysts

Fig. 6 shows the UV-vis diffuse reflectance spectra (UV-vis DRS) of the different TiO$_2$ and g-C$_3$N$_4$ nanocomposites and their precursors. The raw TiO$_2$ and TiO$_2$-cal have ultraviolet light absorption almost below 400 nm, while the hydrogenated H–TiO$_2$ shows extended weak absorption in the range of 400–600 nm, characteristic of reported black TiO$_2$ nanomaterials.[7] All g-C$_3$N$_4$ samples have much greater absorbance in the visible light range of 400–600 nm. The post-treatment by mild oxidation in H$_2$O does not influence much the absorption, whereas the treatment by acid slightly blue-shifts the absorption.[45,46] After combining TiO$_2$ with g-C$_3$N$_4$ in

Fig. 5 Ti 2p, N 1s, O 1s and C 1s XPS spectra of the three nanocomposites (O–CN/TiO$_2$, CN/TiO$_2$-cal and H–CN/H–TiO$_2$) and the precursors (TiO$_2$, CN and O–CN).

This journal is © The Royal Society of Chemistry 2019

Catal. Sci. Technol., 2019, **9**, 75–85 | 81
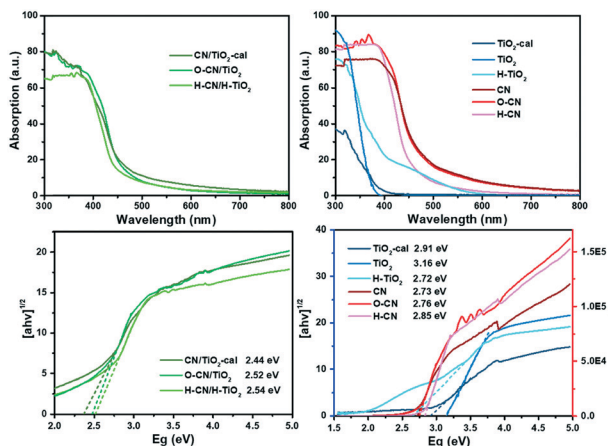
Fig. 6 UV-vis DRS and the corresponding plots of $(\alpha h\nu)^2$ or $(\alpha h\nu)^{1/2}$ versus photon energy ($h\nu$) of the three composite samples (O–CN/TiO$_2$, CN/TiO$_2$-cal and H–CN/H–TiO$_2$) and the precursors (TiO$_2$, TiO$_2$-cal, H–TiO$_2$, CN, O–CN and H–CN). The bandgap energies are indicated in the figure.

three ways, the absorption in both the visible and ultraviolet light regions is significantly enhanced. Compared to the individual precursors, the nanocomposites show the both characteristic light responses of TiO$_2$ and g-C$_3$N$_4$. The spectra of the three nanocomposites are close to each other, not a simple superposition of each precursor, which implies the synergistic effect between g-C$_3$N$_4$ and TiO$_2$ to enhance the photo-absorption performance due to the construction of heterojunctions.

The band gap energy (E_g) was calculated according to the plots of transformed Kubelka-Munk (KM) function versus the light energy for the samples, as shown in Fig. 6. The function is $(\alpha h\nu)^2 = A(h\nu - E_g)$ or $(\alpha h\nu)^{1/2} = A(h\nu - E_g)$ for direct or indirect transition semiconductors, respectively, where A is a constant, $h\nu$ is the photon energy, h is Planck's constant, ν is the frequency of vibration, and α is the absorption coefficient.[22,38] The estimated band gap energy of TiO$_2$-cal (2.91 eV) is smaller than that of raw TiO$_2$ nanosheets (3.16 eV), due to the increased crystallinity.[48] The hydrogenation of TiO$_2$ further narrowed the E_g to 2.72 eV, due to the increase of oxygen vacancies and Ti^{3+} concentration.[44] The band gap energies of CN, O–CN and H–CN are 2.73, 2.76 and 2.85, respectively, consistent with the reported values.[45,46] The slight alterations are ascribed to the introduction of electron-withdrawing O groups and the quantum confinement effect, respectively.[45,46] The band gap energies for the nanocomposites O–CN/TiO$_2$, CN/TiO$_2$-cal and H–CN/H–TiO$_2$ are 2.44, 2.52 and 2.54, respectively, which are lower than those of the precursors of TiO$_2$ or g-C$_3$N$_4$. These results indicate that the photo-excitation occurs between the valence band (VB) of g-C$_3$N$_4$ and the conduction band (CB) of the TiO$_2$ part in these nanocomposites with efficient 2D/2D interfacial contact, ensuring the high light absorption efficiency and therefore the improved photocatalytic performance for H$_2$ evolution.

The photocatalytic activity of the three TiO$_2$ and g-C$_3$N$_4$ nanocomposites, the physically mixed sample and the precursors was assessed by photocatalytic hydrogen evolution under visible light irradiation ($\lambda > 400$ nm) with 20 vol% TEOA as the sacrificial agent and 3 wt% Pt as the co-catalyst, as shown in Fig. 7. The raw TiO$_2$ nanosheets show no photocatalytic activity due to the zero photo-absorption below 400 nm. The hydrogenated H–TiO$_2$ also shows a negligible H$_2$ evolution rate, perhaps due to the weak visible-light absorption. For g-C$_3$N$_4$ precursors, the time evolution curve for H$_2$ production of O–CN almost overlaps with CN, while the activity of H–CN is about 1.5 times that of CN in terms of the average H$_2$ evolution rate in the time span of 4 h. The reason could lie in the subtle modification of the band structure in O–CN; the influence on the band structure after the introduction of oxygen into g-C$_3$N$_4$ remains controversial in the literature.[45,51,52] The enhancement in the catalytic activity after acid treatment could be explained by the increased favorable defects, which expose more activity sites and decrease recombination sites.[46] The simple physical mixture of TiO$_2$ and g-C$_3$N$_4$ would result in exactly half the H$_2$ evolution activity compared to the pure g-C$_3$N$_4$, as observed with the O–CN TiO$_2$ mixed sample and O–CN. Weak van der Waals interaction occurs in the "heterojunction" of the physical mixture, but does not accelerate the photocatalytic process.

The hybridization with TiO$_2$ forming the three nanocomposites, however, significantly enhances the photocatalytic activity for H$_2$ evolution, in comparison with the physical mixture of the corresponding TiO$_2$ and g-C$_3$N$_4$ precursors, indicating the synergic interaction between the two components across the interface. Among the three nanocomposites, O–CN/TiO$_2$ shows the highest H$_2$ evolution rate, reaching a kinetic rate of 587 μmol g^1 h^{-1}, which is about 6.1 times that of the physical mixture. The photocatalytic activity stability of the O–CN/TiO$_2$ nanocomposite was evaluated by extending the photo-irradiation time to 14 h. As shown in Fig. S4,† the average rate of H$_2$ formation is 566 μmol g^{-1} h^{-1}, close to the average rate during the initial 4 h, indicating the maintenance of excellent photocatalytic activity for H$_2$ evolution on
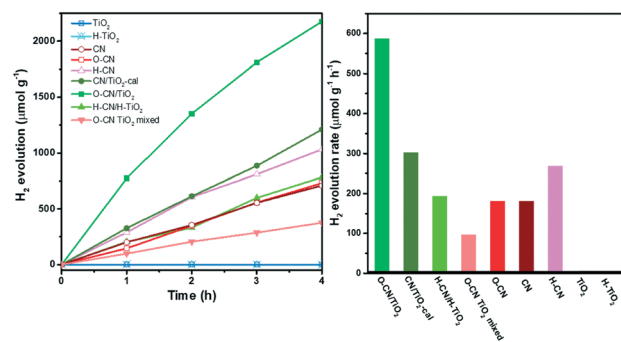
Fig. 7 H$_2$ evolution of the three composite samples (O–CN/TiO$_2$, CN/TiO$_2$-cal and H–CN/H–TiO$_2$), the physically mixed sample (O–CN TiO$_2$ mixed) and the precursors (TiO$_2$, H–TiO$_2$, CN, O–CN and H–CN) under visible light irradiation (left). The corresponding H$_2$ evolution rates (right).

82 | Catal. Sci. Technol., 2019, 9, 75–85

This journal is © The Royal Society of Chemistry 2019

O–CN/TiO$_2$. The increase factors for the photocatalytic activity of CN/TiO$_2$-cal and H–CN/H–TiO$_2$ are 3.4 and 1.4 times, respectively, relative to the physical mixture. Though the surface area of CN/TiO$_2$-cal is the lowest among the three composites, the remarkable enhancement highlights the importance of forming covalent Ti–O–N bonds at the interface of TiO$_2$ and g-C$_3$N$_4$ for the rapid charge carrier transfer and separation. The charge-induced aggregated H–CN/H–TiO$_2$ sample, with a medium surface area and close 2D/2D face-to-face contact, does not avoid electron–hole recombination through electrostatic interaction as efficiently as through the covalent chemical bonds.

The PL spectra of the nanocomposite samples and the precursors are shown in Fig. 8, revealing the recombination of charge carriers mainly in the g-C$_3$N$_4$ part.[29,34] The highest PL emission intensity is observed with the pristine CN, indicating the most severe recombination of electron–hole pairs, as a result of n–π* electronic transitions involving lone pairs of N atoms.[20,23] The peak position is located at *ca.* 460 nm (*i.e.*, 2.7 eV), in conformity with the band gap energy derived from its UV-vis DRS spectrum.[35] The PL intensities decrease after the pretreatment of CN, consistent with previously reported results.[45,46] The formation of the three nanocomposites with TiO$_2$ further decreases the PL intensity, which is caused by the efficient separation of photogenerated electron–hole pairs between TiO$_2$ and g-C$_3$N$_4$.[20,34,53] The degree of PL quenching is in accordance with the photocatalytic hydrogen evolution results. The interfacial chemical bonds, *i.e.*, Ti–O–N, in O–CN/TiO$_2$ and CN/TiO$_2$-cal most conspicuously facilitate the photogenerated charge separation and transfer, thereby effectively reducing the PL intensity and increasing the lifetime of photogenerated electrons and holes for the most prominently accelerated photocatalytic reactions. The recombination of photogenerated charge carriers is hardly inhibited in the O–CN TiO$_2$ mixed sample and slightly retarded in H–CN/H–TiO$_2$, reflecting the dependence of PL intensity on the inter-

action modes between TiO$_2$ and g-C$_3$N$_4$, which also determines the photocatalytic performance.
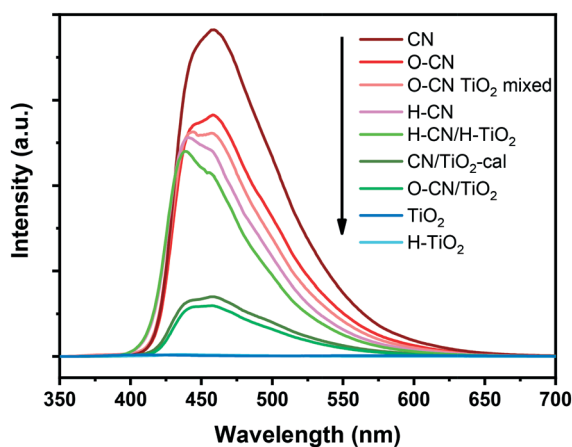
The establishment of an intimate interfacial contact between TiO$_2$ nanosheets and g-C$_3$N$_4$ is crucial to achieving high photocatalytic activity for H$_2$ evolution. Scheme 2 shows a tentative photocatalytic H$_2$ evolution mechanism catalyzed by TiO$_2$ and g-C$_3$N$_4$ nanocomposites with deposited Pt under visible light irradiation. TiO$_2$ nanosheets have the VB and CB at about 2.9 and −0.3 eV (*vs.* NHE), respectively.[30,34] The calcination or hydrogenation by NaBH$_4$ do not turn TiO$_2$ into a strong visible-light absorber. Calcination largely reduces the surface area though the crystallinity increases and P123 organic residues are removed. The VB and CB of CN are located at about 1.5 and −1.2 eV, respectively.[16,30,46] The mild oxidation or acid treatment results in slight modification of the band structure.[46,52] These treatments and calcination[50] indeed exfoliate CN, but still contribute a minor surface area to the nanocomposites with TiO$_2$.

In the presence of the three TiO$_2$ and g-C$_3$N$_4$ nanocomposites, at first, electrons in the VB of g-C$_3$N$_4$ are excited to its CB under visible-light irradiation, forming the electron–hole pairs. The electrons in the CB of g-C$_3$N$_4$ rapidly transfer to the CB of TiO$_2$ *via* the interfacial contact through either the covalent Ti–O–N bonds (in O–CN/TiO$_2$ and CN/TiO$_2$-cal) or the electrostatic Coulombic interaction (in H–CN/H–TiO$_2$), realizing the efficient separation of photo-induced electrons and holes. The holes flowing from the VB of TiO$_2$ (2.9 eV) to the VB of g-C$_3$N$_4$ (1.5 eV) are captured by TEOA. Simultaneously, the electrons flowing from the CB of g-C$_3$N$_4$ (−1.2 eV) to the CB of TiO$_2$ (−0.3 eV) transfer to Pt for reduction of protons to H$_2$. The Pt co-catalyst easily sinks the accumulated electrons, avoiding the excessive accumulation and recombination of charge carriers.[12,19,49] Pt mainly deposits on the surface of TiO$_2$ due to its large surface area from its ultrathin 2D structure. Therefore, the facilitated electron-transfer across the g-C$_3$N$_4$ and TiO$_2$ interface and the large surface area of the TiO$_2$ phase are the two most important factors for improving the photocatalytic efficiency of H$_2$ evolution.

Fig. 8 PL spectra of the three composite samples (O–CN/TiO$_2$, CN/TiO$_2$-cal and H–CN/H–TiO$_2$), the physically mixed sample (O–CN TiO$_2$ mixed) and the precursors (TiO$_2$, H–TiO$_2$, CN, O–CN and H–CN) under 330 nm excitation.
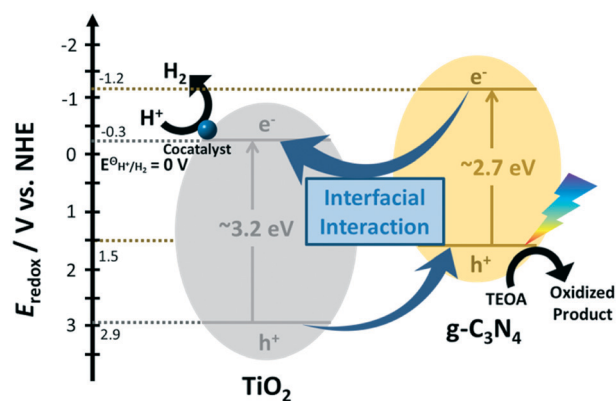
Scheme 2 The energy diagram of the TiO$_2$ and g-C$_3$N$_4$ composites for photocatalytic H$_2$ evolution under visible light irradiation.

Conclusions

In summary, three distinct and typical approaches were applied to fabricate TiO_2 and g-C_3N_4 2D/2D nanocomposites, *i.e.*, solvothermal treatment, co-calcination and surface charge-induced heteroaggregation. The resultant three heterostructures exhibit higher photocatalytic activities towards the hydrogen evolution reaction under visible light irradiation, in comparison with the physical mixture of the corresponding g-C_3N_4 and TiO_2 nanosheets, with an enhancement factor of 1.4–6.1. According to the analyses of the physicochemical properties, the formation of covalent Ti–O–N is evidenced to more efficiently facilitate the migration and separation of photo-induced charge carriers compared to electrostatic interactions, thus being more beneficial for H_2 evolution. In addition, the maintenance of the large surface area outweighs the surface-cleanliness and crystallinity of the TiO_2 component in the composites in terms of the photocatalytic H_2 evolution activity. The well-designed comparative experiments and detailed characterization in this work may pave the way for rational design and synthesis of other composite materials with well-defined heterostructures for versatile applications.

Conflicts of interest

There are no conflicts to declare.

Acknowledgements

References

1 C. Acar, I. Dincer and G. F. Naterer, *Int. J. Energy Res.*, 2016, **40**, 1449–1473.

2 J. A. Turner, *Science*, 2004, **305**, 972–974.

3 P. Lianos, *Appl. Catal., B*, 2017, **210**, 235–254.

4 J. Schneider, M. Matsuoka, M. Takeuchi, J. Zhang, Y. Horiuchi, M. Anpo and D. W. Bahnemann, *Chem. Rev.*, 2014, **114**, 9919–9986.

5 S. Dong, J. Feng, M. Fan, Y. Pi, L. Hu, X. Han, M. Liu, J. Sun and J. Sun, *RSC Adv.*, 2015, **5**, 14610–14630.

6 A. Fujishima and K. Honda, *Nature*, 1972, **238**, 37–38.

7 S. G. Ullattil, S. B. Narendranath, S. C. Pillai and P. Periyat, *Chem. Eng. J.*, 2018, **343**, 708–736.

8 S. Chu, Y. Wang, Y. Guo, J. Feng, C. Wang, W. Luo, X. Fan and Z. Zou, *ACS Catal.*, 2013, **3**, 912–919.

9 W. Ong, L. Tan, Y. H. Ng, S. Yong and S. Chai, *Chem. Rev.*, 2016, **116**, 7159–7329.

10 J. Zhang, Y. Chen and X. Wang, *Energy Environ. Sci.*, 2015, **8**, 3092–3108.

11 S. Martha, S. Mansingh, K. M. Parida and A. Thirumurugan, *Mater. Chem. Front.*, 2017, **1**, 1641–1653.

12 S. Patnaik, S. Martha and K. M. Parida, *RSC Adv.*, 2016, **6**, 46929–46951.

13 S. Patnaik, S. Martha, S. Acharya and K. M. Parida, *Inorg. Chem. Front.*, 2016, **3**, 336–347.

14 S. Martha, A. Nashim and K. M. Parida, *J. Mater. Chem. A*, 2013, **1**, 7816–7824.

15 G. T. S. T. Da Silva, K. T. G. Carvalho, O. F. Lopes and C. Ribeiro, *Appl. Catal., B*, 2017, **216**, 70–79.

16 Q. Zhang, S. Yuan, B. Xu, Y. Xu, K. Cao, Z. Jin, C. Qiu, M. Zhang, C. Su and T. Ohno, *Catal. Today*, 2018, **315**, 184–193.

17 Y. Hong, Z. Fang, B. Yin, B. Luo, Y. Zhao, W. Shi and C. Li, *Int. J. Hydrogen Energy*, 2017, **42**, 6738–6745.

18 Y. Wang, Q. Wang, X. Zhan, F. Wang, M. Safdar and J. He, *Nanoscale*, 2013, **5**, 8326–8339.

19 T. Su, Q. Shao, Z. Qin, Z. Guo and Z. Wu, *ACS Catal.*, 2018, **8**, 2253–2276.

20 Z. Lu, L. Zeng, W. Song, Z. Qin, D. Zeng and C. Xie, *Appl. Catal., B*, 2017, **202**, 489–499.

21 K. Li, Z. Huang, X. Zeng, B. Huang, S. Gao and J. Lu, *ACS Appl. Mater. Interfaces*, 2017, **9**, 11577–11586.

22 F. Chang, J. Zhang, Y. Xie, J. Chen, C. Li, J. Wang, J. Luo, B. Deng and X. Hu, *Appl. Surf. Sci.*, 2014, **311**, 574–581.

23 J. Ma, X. Tan, F. Jiang and T. Yu, *Catal. Sci. Technol.*, 2017, **7**, 3275–3282.

24 R. Zhong, Z. Zhang, H. Yi, L. Zeng, C. Tang, L. Huang and M. Gu, *Appl. Catal., B*, 2018, **237**, 1130–1138.

25 W. Gu, F. Lu, C. Wang, S. Kuga, L. Wu, Y. Huang and M. Wu, *ACS Appl. Mater. Interfaces*, 2017, **9**, 28674–28684.

26 K. Li, S. Gao, Q. Wang, H. Xu, Z. Wang, B. Huang, Y. Dai and J. Lu, *ACS Appl. Mater. Interfaces*, 2015, **7**, 9023–9030.

27 S. Zhou, Y. Liu, J. Li, Y. Wang, G. Jiang, Z. Zhao, D. Wang, A. Duan, J. Liu and Y. Wei, *Appl. Catal., B*, 2014, **158–159**, 20–29.

28 N. Boonprakob, N. Wetchakun, S. Phanichphant, D. Waxler, P. Sherrell, A. Nattestad, J. Chen and B. Inceesungvorn, *J. Colloid Interface Sci.*, 2014, **417**, 402–409.

29 W. Wang, J. Fang, S. Shao, M. Lai and C. Lu, *Appl. Catal., B*, 2017, **217**, 57–64.

30 S. Pany and K. M. Parida, *Phys. Chem. Chem. Phys.*, 2015, **17**, 8070–8077.

31 Y. Wang, W. Yang, X. Chen, J. Wang and Y. Zhu, *Appl. Catal., B*, 2018, **220**, 337–347.

32 J. Li, M. Zhang, Q. Li and J. Yang, *Appl. Surf. Sci.*, 2017, **391**, 184–193.

33 J. Li, M. Zhang, X. Li, Q. Li and J. Yang, *Appl. Catal., B*, 2017, **212**, 106–114.

34 M. Reli, P. Huo, M. Šihor, N. Ambrožová, I. Troppová, L. Matějová, J. Lang, L. Svoboda, P. Kuśtrowski, M. Ritz, P. Praus and K. Kočí, *J. Phys. Chem. A*, 2016, **120**, 8564–8573.

35 S. Patnaik, S. Martha, G. Madras and K. M. Parida, *Phys. Chem. Chem. Phys.*, 2016, **18**, 28502–28514.

84 | *Catal. Sci. Technol.*, 2019, **9**, 75–85

This journal is © The Royal Society of Chemistry 2019

36 W. Ong, L. Tan, S. Chai, S. Yong and A. R. Mohamed, *Nano Energy*, 2015, **13**, 757–770.

37 L. Yuan, M. Yang and Y. Xu, *Nanoscale*, 2014, **6**, 6335–6345.

38 Y. Chen, W. Huang, D. He, Y. Situ and H. Huang, *ACS Appl. Mater. Interfaces*, 2014, **6**, 14405–14414.

39 S. Patnaik, G. Swain and K. M. Parida, *Nanoscale*, 2018, **10**, 5950–5964.

40 S. Liu, F. Li, Y. Li, Y. Hao, X. Wang, B. Li and R. Liu, *Appl. Catal., B*, 2017, **212**, 115–128.

41 G. Jiang, K. Geng, Y. Wu, Y. Han and X. Shen, *Appl. Catal., B*, 2018, 366–375.

42 S. Patnaik, D. P. Sahoo, L. Mohapatra, S. Martha and K. M. Parida, *Energy Technol.*, 2017, **5**, 1687–1701.

43 Z. Sun, T. Liao, Y. Dou, S. M. Hwang, M. Park, L. Jiang, J. H. Kim and S. X. Dou, *Nat. Commun.*, 2014, **5**, 3813–3821.

44 B. Yan, P. Zhou, Q. Xu, X. Zhou, D. Xu and J. Zhu, *RSC Adv.*, 2016, **6**, 6133–6137.

45 L. Ming, H. Yue, L. Xu and F. Chen, *J. Mater. Chem. A*, 2014, **2**, 19145–19149.

46 C. Dong, Z. Ma, R. Qie, X. Guo, C. Li, R. Wang, Y. Shi, B. Dai and X. Jia, *Appl. Catal., B*, 2017, **217**, 629–636.

47 J. Xu, Y. Chen, Y. Hong, H. Zheng, D. Ma, B. Xue and Y. Li, *Appl. Catal., A*, 2018, **549**, 31–39.

48 J. Yang, Y. Jiang, L. Li, E. Muhire and M. Gao, *Nanoscale*, 2016, **8**, 8170–8177.

49 Z. Zhang, L. Lu, Z. Lv, Y. Chen, H. Jin, S. Hou, L. Qiu, L. Duan, J. Liu and K. Dai, *Appl. Catal., B*, 2018, **232**, 384–390.

50 S. C. Yan, Z. S. Li and Z. G. Zou, *Langmuir*, 2009, **25**, 10397–10401.

51 Y. Huang, Y. Wang, Y. Bi, J. Jin, M. F. Ehsan, M. Fu and T. He, *RSC Adv.*, 2015, **5**, 33254–33261.

52 C. Wang, H. Fan, X. Ren, J. Ma, J. Fang and W. Wang, *ChemSusChem*, 2018, **11**, 700–708.

53 S. Nayak, L. Mohapatra and K. Parida, *J. Mater. Chem. A*, 2015, **3**, 18622–18635.

This journal is © The Royal Society of Chemistry 2019

Catal. Sci. Technol., 2019, **9**, 75–85 | **85**